Quantitative image reconstruction for small-animal SPECT imaging including resolution recovery, scatter correction and attenuation correction

Dareyni, Amir; Alikhani, Amirhossein; Ghorbanzadeh, Mohammad; Rezaee, Salman; Farahani, Mohammad Hossein; Teimourianfard, Behnoush; Zaidi, Habib; Ay, Mohammad Reza

Published in:
Physica Medica

DOI:
10.1016/j.ejmp.2026.105761

Publication date:
2026

Document version:
Final published version

Physica Medica 144 (2026) 105761

Contents lists available at ScienceDirect

Physica Medica

journal homepage: www.elsevier.com/locate/ejmp

Quantitative image reconstruction for small-animal SPECT imaging including resolution recovery, scatter correction and attenuation correction

Amir Dareyni [a,b], Amirhossein Alikhani [a], Mohammad Ghorbanzadeh [a], Salman Rezaee [a], Mohammad Hossein Farahani [a], Behnoush Teimourianfard [a], Habib Zaidi [c,d,e,f,*], Mohammad Reza Ay [a,b,*]

[a] Research Center for Molecular and Cellular Imaging (RCMCI), Advanced Medical Technologies and Equipment Institute (AMTEI), Tehran University of Medical Sciences (TUMS), Tehran, Iran
[b] Department of Medical Physics and Biomedical Engineering, Tehran University of Medical Sciences, Tehran, Iran
[c] Division of Nuclear Medicine & Molecular Imaging, Geneva University Hospital, Geneva CH-1211, Switzerland
[d] Department of Nuclear Medicine and Molecular Imaging, University of Groningen, University Medical Center Groningen, Groningen, Netherlands
[e] Department of Nuclear Medicine, University of Southern Denmark, Odense, Denmark
[f] University Research and Innovation Center, Óbuda University, Budapest, Hungary

ARTICLE INFO

Keywords:
SPECT
Preclinical imaging
Quantitative image reconstruction
Attenuation correction
Scatter correction
Resolution recovery

ABSTRACT

Background: High-resolution small-animal SPECT imaging plays a pivotal role in preclinical research by enabling quantitative visualization of radiopharmaceutical distribution in animal models. However, challenges, including physical degrading factors, such as photon attenuation, scattering, and limited spatial resolution hinder SPECT's quantitative accuracy. Advanced reconstruction algorithms are essential to mitigate these effects and enhance image fidelity.

Methods: We developed a quantitative iterative reconstruction algorithm for the developed silicon photomultipliers (SiPMs)-based HiReSPECT II preclinical SPECT system, incorporating resolution recovery, attenuation correction, and scatter compensation. Resolution recovery was modelled using a distance-dependent Gaussian collimator-detector response (CDR). Attenuation correction was implemented via binary attenuation maps with photon path-length calculation using Siddon's ray-tracing method. Scatter correction was performed on list-mode data by estimating and subtracting scattered events using the Dual-Energy Window (DEW) technique. The reconstructed images were calibrated to absolute radiotracer concentration units. Quantitative imaging performance was validated using uniformity and NEMA NU 4–2008 image quality phantoms, followed by *in vivo* mouse imaging studies.

Results: The proposed algorithm significantly enhanced image quality and quantitative accuracy. Resolution recovery improved sharpness, while scatter and attenuation corrections minimized artifacts and ensured uniformity. Key metrics demonstrated substantial improvements in contrast, uniformity and resolution. Quantitative accuracy also significantly improved.

Conclusion: Incorporating resolution recovery, scatter correction, and attenuation correction into preclinical SPECT image reconstruction is critical for achieving high quantitative accuracy. The integration of these techniques in systems, such as HiReSPECT II, establishes a new benchmark for preclinical imaging, facilitating radiotracer development and advancing translational research.

1. Introduction

Single-Photon Emission Computed Tomography (SPECT) is a nuclear medical imaging technique that enables three-dimensional visualization of radiotracer distribution by detecting emitted gamma rays [1–3]. Due to its ability to quantify physiological processes, such as perfusion, metabolism, and receptor density, SPECT has become a cornerstone in both clinical diagnostics and preclinical research [4–6]. In translational

* Corresponding authors at: Geneva University Hospital, Division of Nuclear Medicine and Molecular Imaging, CH-1211 Geneva, Switzerland (H. Zaidi). Department of Medical Physics and Biomedical Engineering, School of Medicine, Tehran University of Medical Sciences, Tehran, Iran (M. Reza).
E-mail addresses: habib.zaidi@hug.ch (H. Zaidi), mohammadreza_ay@sina.tums.ac.ir (M.R. Ay).

https://doi.org/10.1016/j.ejmp.2026.105761
Received 22 December 2025; Received in revised form 20 February 2026; Accepted 7 March 2026
Available online 12 March 2026

small-animal imaging, SPECT plays a critical role in studying disease mechanisms, drug development [7,8], and therapeutic interventions, particularly in cardiology [9,10], oncology,and neuroscience [11]. However, physical limitations of SPECT [12]—including finite spatial resolution, photon attenuation, and Compton scattering—pose significant challenges in achieving quantitative accuracy, especially in small-animal studies where high resolution and sensitivity are essential.

The primary factors degrading SPECT image quality include collimator-detector response (CDR), which introduces spatial blurring and limits resolution; attenuation effects where gamma photons are absorbed or scattered as they traverse tissue, leading to non-uniform signal loss; and Compton scattering, which contributes to background noise and reduces image contrast [13]. Early reconstruction methods, such as filtered backprojection (FBP), limited by noise amplification and an inability to model these physical effects [14]. Iterative reconstruction techniques, including maximum likelihood expectation maximization (MLEM) [15] and ordered subsets – expectation maximization (OSEM) [16], significantly improved quantitative accuracy by incorporating system models and physical corrections. Recent advances have further refined these methods through resolution recovery techniques (e.g., distance-dependent CDR modelling [17,18] or Monte Carlo-based blurring kernels [19,20]), CT-derived attenuation correction [21,22] and advanced scatter correction methods. such as Monte Carlo simulation [23,24] or energy-window-based approaches (dual-energy window (DEW)/triple-energy window (TEW)) [25–29].

In addition to earlier work demonstrating the benefits of physical corrections for quantitative SPECT imaging, recent methodological advances continue to refine both resolution modelling and scatter compensation strategies. Polson *et al.* proposed a computationally efficient collimator–detector response (CDR) compensation method using one–dimensional convolutions and rotations that significantly reduce computational cost while maintaining quantitative fidelity compared to traditional two–dimensional models, illustrating ongoing interest in efficient resolution recovery modelling [30]. Ebrahimifard *et al.* investigated the impact of reconstruction algorithms incorporating enhanced resolution modelling on recovery coefficients in phantom studies, highlighting how physics–based PSF/CDR models influence quantification of small structures [31]. Concurrently, recent evaluations of energy window–based scatter correction techniques, including comparisons between dual-energy window (DEW) and triple-energy window (TEW) methods, have demonstrated that optimized scatter estimation improves contrast recovery and uniformity, with TEW showing advantages under specific conditions [32]. Additional studies in cardiac and bone SPECT imaging have quantitatively shown that both DEW and TEW reduce scatter–related bias relative to uncorrected data, further supporting the continued relevance of energy window–based approaches for quantitative SPECT [33]. These contemporary contributions corroborate the importance of integrating advanced resolution modelling and tailored scatter compensation within iterative reconstruction frameworks, situating the present work within current research efforts aiming at enhancing quantification and image quality in SPECT.

Despite substantial advances in small-animal SPECT imaging, robust quantitative performance in preclinical settings remains challenging due to photon attenuation, scatter, and limited system resolution. Here, a complete reconstruction framework was developed from the ground up, incorporating attenuation correction, scatter correction, and resolution recovery directly into the reconstruction process. All correction models and the core projector–backprojector pair were implemented independently, without reliance on external tools or post-processing modules.

A key aspect of this study is the full integration of the proposed framework into the reconstruction pipeline of a commercially available high-resolution preclinical SPECT system developed by our group for the biomedical research market. This real-world deployment on the operational industrial platform enabled comprehensive evaluation using physical phantoms and animal datasets acquired at multiple preclinical imaging facilities, providing direct comparison with the manufacturer's standard reconstruction under routine operating conditions.

This integration into an operational commercial system facilitates the assessment of the method's performance in authentic preclinical environments and supports its potential adoption in research settings that rely on established small-animal SPECT instrumentation.

This study presents a quantitative reconstruction algorithm for small-animal SPECT that incorporates resolution recovery using collimator–detector response (CDR) modelling directly within the projector–backprojector pair, attenuation correction, and an energy-based scatter correction method into a unified statistical iterative framework. Performance is evaluated through experimental phantom studies and *in vivo* small-animal imaging. By integrating these physical corrections within the reconstruction process, the proposed approach seeks to improve quantitative accuracy and spatial resolution, thereby strengthening the role of preclinical SPECT in drug development and precision medicine applications.

2. Materials and methods

2.1. System specifications

The SiPM-based HiReSPECT II scanner is a dual-detector SPECT system designed for high-resolution imaging developed in our laboratory. This system is an upgraded version of the previously reported HiReSPECT I platform [34], incorporating enhancements in detector configuration, acquisition electronics, and reconstruction framework. A detailed technical description of the HiReSPECT II system will be provided in a future article. Each detector head is equipped with interchangeable collimators, though the current configuration employs parallel-hole collimators for optimal sensitivity-resolution tradeoffs. The system supports adjustable radii of rotation (ROR), enabling detector positioning optimization for specific imaging tasks through synchronized radial motion of both heads. The system includes a table designed to support the sample, which can translate over a wide range along the z-axis of the scanner.

The gantry assembly, which integrates the detectors, collimators, and readout electronics, performs step-and-shoot rotations around the specimen to acquire 2D projection data at predefined angular intervals. Each detector module incorporates four Silicon Photomultiplier (SiPM) blocks arranged in a surface-mount technology (SMT) configuration. These SiPM (SensL, Ireland) arrays are optically coupled to a pixelated Cesium Iodide (CsI) scintillation crystal (EBCO Optoelectronic Technology, Shanghai, China) (68 × 68 array; 1.3 × 1.3 × 5 mm^3 pixel dimensions). The detector face features a lead collimator with hexagonal hole geometry (Nuclear Fields Pty Ltd, Australia), characterized by 1.5 mm apertures, 0.2 mm septa, and 35 mm thickness – parameters optimized for 100–200 keV gamma ray detection (Fig. 1).

2.2. Data readout and calibration

SPECT systems capture detailed information for every detected photon, such as its interaction coordinates within the detector, the energy deposited during detection, and timing labels called timestamps. These parameters are systematically compiled into a sequential data structure known as *list-mode (LM)* format, which preserves the temporal and spatial fidelity of each event. The LM data packets are then transmitted to the acquisition computer using the User Datagram Protocol (UDP), with transfer rates typically ranging between 10 and 50 Mbps, depending on system configuration and detector specifications.

To facilitate real-time processing, a multi-threaded acquisition pipeline was designed to manage high-speed data reception, perform essential calibrations, and verify data integrity. The calibration phase incorporates corrections for spatial linearity, energy response, and detector uniformity, ensuring that the resulting projections meet the necessary quantitative standards for clinical or research applications. By maintaining synchronization and minimizing processing delays, this

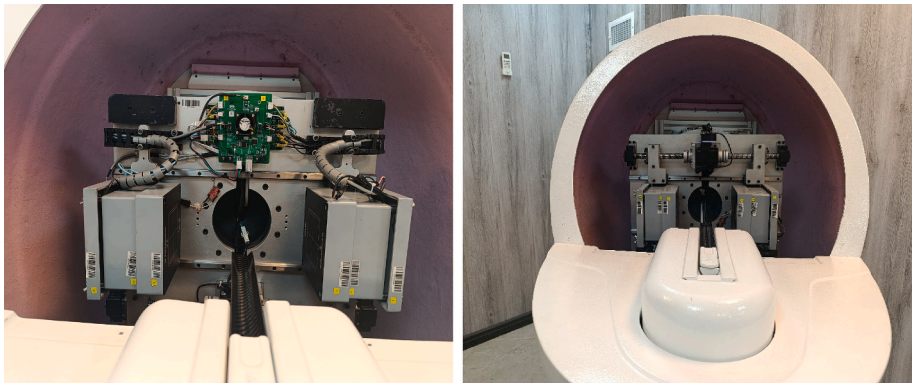

Fig. 1. Photographs of the HiReSPECT II animal SPECT scanner.

pipeline enhances the reliability of the acquired data for downstream analysis.

2.3. Reconstruction framework

2.3.1. Forward projection modelling – System matrix

Image reconstruction, treated as an inverse problem, can be formulated as a system of linear equations.

$$g = H \times \mathrm{f} \tag{1}$$

In this context, **g** represents an **m**-dimensional vector that encodes the 2D data acquired by the scanner, while **f** is an **n**-dimensional vector representing the object being imaged. The system matrix **H** captures the characteristics of the imaging system and models the forward projection process, mapping the object data **f** to the measured data **g**. The matrix **H** also serves as a back-projection operator when its transpose, $\mathbf{H}^{\mathrm{T}}$, is applied to the measured data **g**. This forward projection and back-projection pair forms the foundation of iterative reconstruction algorithms, enabling the iterative refinement of the object estimate **f**.

The system matrix is constructed by first determining the dimensions of the object, voxelizing it, and specifying the number of elements (N), detector components (m), and projection angles (K). Projections, which represent the total number of gamma photons emitted along a specific angle and detected along a single line, are measured at each angle for each individual voxel to organize the data. Forward projection algorithms, developed from scratch in Python, leveraging NumPy for array operations and vectorized calculations, and SciPy's sparse matrix functionality to efficiently store the large system matrix. A matrix of size (K × m × N) is initialized with zeros. For each voxel, its corresponding projection is calculated and stored as a column vector in the matrix. This process is repeated for all *N* voxels, with each projection placed in subsequent columns. The result is a fully populated system matrix, generated using Python, for further reconstruction.

2.4. Reconstruction algorithm

In this study, we developed an MLEM-based image reconstruction algorithm that utilizes the previously described system matrix as both projector and back-projector. MLEM aims to iteratively estimate the most likely object distribution from the 2D projection data. The process begins with an initial low-frequency guess, typically a matrix of ones, as the starting estimate. To compare this estimate with the measured data, the estimate must first be transformed into projection space using the system matrix as forward projector to simulate the forward projection process. The algorithm then computes the error projection by dividing the measured projection by the calculated one. Using this error projection, the system matrix acts as a back-projector to generate an error image, which is used to update the estimate by multiplying it with the current image. This iterative process is repeated for a predefined number of iterations or until convergence is achieved. The MLEM algorithm is formulated as:

$$\lambda_j^{(k+1)} = \frac{\lambda_j^{(k)}}{\sum_i a_{ij}} \Sigma_i \left(\frac{y_i}{\Sigma_l a_{il} . \lambda_l^{(k)}} \right) a_{ij} \tag{2}$$

where $\lambda_j^{(k)}$ denotes the estimated activity of voxel *j* at iteration *k*, updated to $\lambda_j^{(k+1)}$ in the next step. The measured projection data in detector bin *i* is represented by y_i. The system matrix element a_{ij} defines the probability that an emission from voxel *j* is detected in bin *i*. The normalization term $\sum_i a_{ij}$ accounts for the total contribution of voxel *j* across all bins. The denominator $\sum_l a_{il} \lambda_l^{(k)}$, where *l* indexes all voxels, represents the forward projection estimate of bin *i*.

2.5. Resolution recovery

The primary cause of spatial resolution degradation in SPECT imaging is the collimator, which exhibits a direct dependency on the distance from the object being image. In this context, the CDR characterizes the finite dispersion of photons originating from the patient. Mathematically, this relationship can be expressed as:

$$d(\vec{x}, \vec{r}) = \iint i(\vec{x}, \vec{x'})(g(\vec{x'}, \vec{r}) + p(\vec{x'}, \vec{r}) + s(\vec{x'}, \vec{r}))d\vec{x'} \tag{3}$$

$i(\vec{x}, \vec{x'})$ is the intrinsic point-source response function that describes the probability that a photon incident at position $\vec{x'}$ is detected at $\vec{x}$, $g(\vec{x'}, \vec{r}), p(\vec{x'}, \vec{r})$ and $s(\vec{x'}, \vec{r})$ are geometric, septal penetration and septal scatter response functions describing the probability that a photon emitted at $\vec{r}$ will pass through the collimator holes.

Incorporating the CDR into system modelling via the system matrix provides a mechanism to estimate the position-dependent blurring, rather than assuming uniform degradation across the field-of-view. Iterative reconstruction methods allow for embedding CDR modelling within the system matrix, resulting in a representation that more accurately reflects the imaging system's physics. This requires computing the CDR for all pixels in the image. Since CDR varies with distance, all pixels within a single imaging plane can be approximated to share the same CDR, significantly reducing computational complexity.

To empirically determine the CDR, a rod source with a known activity was positioned at varying distances from the collimator (30 mm, 45 mm, 60 mm, 75 mm, and 90 mm). At each distance, the CDR was quantified for each plane using the full-width-at-half-maximum (FWHM) metric based on NEMA standards guideline. To achieve a continuous representation of the measurements rather than relying on

discrete distances, a Gaussian function was fitted to the data (Eq. (4). This approach facilitated the estimation of statistical distribution parameters, enabling interpolation of the CDR at arbitrary distances.

To integrate the CDR into the system modelling process, the Gaussian function's value is applied to account for the influence of a pixel on a specific detector bin based on the pixel-to-detector distance. The resulting system matrix incorporates the CDR model, providing a more accurate depiction of the imaging system's behavior. Using this system matrix enables the reconstruction of images with enhanced resolution, effectively recovering finer details.

$$f(x) = \frac{1}{\sigma\sqrt{2\pi}}\exp\left(-\frac{(x-\mu)^2}{2\sigma^2}\right) \tag{4}$$

$f(x)$ is the Gaussian probability density function. The variable x denotes the random variable under consideration. The parameter μ is the mean, specifying the central location of the distribution, and σ is the standard deviation, controlling the spread of the distribution. The constant π is the mathematical constant pi, ensuring correct normalization.

2.6. Attenuation correction

Photons emitted by an injected radiopharmaceutical attenuate as they traverse tissue, with intensity governed by:

$$\phi = \phi_0 \exp\left[-\int \mu(x,y)dr\right] \tag{5}$$

ϕ denotes the attenuated photon flux after traversing the object, while ϕ_0 is the initial unattenuated photons flux. The function $\mu(x,y)$ represents the linear attenuation coefficient at spatial position (x,y), characterizing the probability of photon interaction per unit path length. The integral $\int \mu(x,y)\,dr$ is evaluated along the photon path r, accounting for the cumulative attenuation encountered.

Attenuation is depth-dependent: photons emitted centrally travel longer paths, suffering greater attenuation than those near the periphery. This results in fewer detected photons from central regions and relative overrepresentation of edge photons, creating non-uniform detection distributions. As an unavoidable effect, this spatial bias compromises quantitative accuracy in reconstructed images. Thus, attenuation correction is essential to mitigate artifacts and ensure diagnostic fidelity.

Chang's attenuation correction method operates under the assumption of uniform tissue attenuation coefficients [35]. Correction factors are computed and applied to the image to account for photon attenuation. To implement this method, the object's boundary must first be accurately contoured in each reconstructed slice, and a uniform attenuation correction factor assigned to all regions. In animal imaging, the body is approximated as water-equivalent, and since the attenuation coefficient of water at 140 keV energy is approximately 0.15 cm^{-1}, this value is assigned to all pixels within the segmented region.

The method calculates the attenuation of photons emitted from each pixel as they travel within the tissue toward the detector. For a given emission angle, the path of each photon is traced to determine which pixels it traverses and the extent of attenuation along its path. This calculation is repeated for all pixels and all projection angles. The resulting attenuation values are stored in the corresponding positions of the system matrix. Siddon's forward projection algorithm is employed to compute the path length through each pixel, thereby enabling the determination of attenuation for photons emitted from any pixel to the detector. The degree of attenuation varies depending on the pixel of origin and its spatial position.

During image reconstruction, the system matrix incorporating these attenuation values is utilized. For each pixel in the reconstructed image, the number of absorbed photons is estimated and added to the reconstructed photon count. This process effectively corrects for attenuation, thus improving the quantitative accuracy of the reconstructed images.

2.7. Siddon forward projection

The algorithm was designed to simulate the imaging process by modelling the propagation of photons from their emission point to the detector [36]. Using a pixel-driven approach, the algorithm traced the trajectory of emitted photons and identified the pixels they traversed. As photons passed through each pixel, the contribution of secondary emissions from that pixel was incorporated into the total photon count recorded by the detector. The detector response was primarily determined by the cumulative values of all pixels along the photon path. More importantly, the algorithm assigned contribution weights to pixels based on the fractional pathlength of the photon within each pixel, rather than assigning equal weights to all pixels along the trajectory.

In practice, the algorithm calculated the pathlength of each photon through every pixel it traversed. This pathlength was then multiplied by the pixel's emission value, representing the number of photons emitted from that pixel. The process was repeated for all pixels along the photon's path, and the resulting photon count detected at a specific angle was computed. This approach allowed for accurate modelling of photon attenuation, ensuring a realistic simulation of the imaging process.

2.8. Scatter correction

Simultaneous acquisition of photopeak and scatter window projections was performed using a 30% energy window centred on the 140 keV photopeak of Tc-99 m, along with a 20% lower scatter window positioned below the photopeak. Scatter correction was implemented using the Dual-Energy Window (DEW) method, in which the scatter distribution estimated from the lower energy window was scaled and subtracted from the photopeak projection. In this approach, a scaling factor K is introduced to compensate for the difference in scatter intensity between the two energy windows. Although a factor of 0.5 is commonly reported for clinical SPECT imaging, this value depends on object size, energy window configuration, and system characteristics. Since the present study involved small-animal imaging with reduced scattering volume, the scatter fraction was expected to be lower than in human studies. The multiplier factor k was determined experimentally using phantom measurements by evaluating reconstructed image contrast and background uniformity across a range of candidate values (0.25–0.5). A value of $k = 0.35$ provided the optimal balance between background suppression and preservation of activity concentration, and was therefore selected for subsequent reconstructions [37]. The corrected projections were subsequently reconstructed using the MLEM algorithm with 20 iterations. Following DEW subtraction, negative pixel values may arise in the scatter-corrected projections due to statistical fluctuations and overestimation of the scatter component. Since the MLEM algorithm assumes non-negative Poisson-distributed projection data, the presence of negative values may lead to numerical instability or reconstruction artifacts.

To ensure compatibility with the Poisson statistical model and maintain numerical stability, a non-negativity constraint was enforced in the projection space. Specifically, any negative pixel values resulting from the DEW subtraction were set to zero prior to reconstruction. This thresholding step preserves the physical validity of the projection data while preventing instability in the iterative reconstruction process.

2.9. Quantification

In SPECT imaging, the voxel values within the image matrix represent the number of counts detected by the gamma camera but do not directly provide quantitative information about the actual concentration of the radiopharmaceutical in the object. To address this limitation, an experimental calibration procedure was conducted to derive a calibration factor (CF) capable of converting voxel values into activity con-

centration, expressed in units of MBq/ml. A point source with a known activity was scanned and reconstructed using the SPECT system. The system calibration factor was then determined using the following formulation, incorporating decay correction to account for the radioactive decay of the source during the experiment:

$$CF = \frac{A}{V.\sum R} \quad (6)$$

In this formulation, A represents the activity of the point source, as measured by a dose calibrator, V denotes the volume of a single voxel, and $\sum R$ corresponds to the total summation of all voxel values within the reconstructed image. By applying the Calibration Factor, derived from this relationship, each voxel value in the SPECT image matrix, initially representing the number of detected photons, can be converted into a quantitative measure of activity concentration. Specifically, multiplying the voxel value by the calibration factor yields the activity concentration in units of MBq/ml, thereby enabling the SPECT image to provide spatially resolved quantitative information about the distribution of the radiopharmaceutical within the object.

The reconstruction package, including resolution recovery, attenuation correction, and scatter correction, was developed in Python. The software was designed with a well-organized structure to ensure clarity and maintainability. A user-friendly graphical interface (GUI) was also implemented to provide an intuitive platform for users to interact with the package, enhancing its accessibility and usability for practical applications.

2.10. Phantom experiments

2.10.1. Animal uniformity phantom

A uniformity phantom is a fillable device designed to ensure a homogeneous radioactive concentration by minimizing air bubbles and preventing material adhesion.

2.10.2. Rod source experiment

To evaluate the resolution recovery algorithm's efficiency, a 3 mm diameter rod source imaged at five distances (30, 45, 60, 75, and 90 mm). Reconstructions were performed using two system matrices—one incorporating the collimator-detector response function (CDRF) and one without. The full width at half maximum (FWHM) computed across all slices for both cases and compared to assess algorithmic performance.

2.10.3. NEMA image quality phantom

To assess the system's quantitative accuracy in more complex structures, the NEMA NU 4–2008 image quality phantom, designed for small-animal imaging, was utilized. This phantom consists of three main components: five rods (hot regions) with diameters ranging from 1 to 5 mm, a uniform section, and two cylindrical cavities (cold regions) with an inner diameter of 8 mm and a length of 15 mm, filled with nonradioactive water and air. The phantom's main body has an inner diameter of 30 mm and was filled with a Tc-99 m solution at a concentration of 13.9 MBq/ml. Scans were performed with a ROR of 50 mm and an acquisition time of 30 s per view. Detailed information about scan parameters are listed in Table 1. The reported pixel size of 1.4×1.4 mm^2 refers to the reconstructed image pixel size after calibration and application of the system zoom factor. This value differs slightly from the 1.3 mm detector crystal pitch specified in the system description, which corresponds to the physical spacing of the detector elements in the 68×68 crystal array. The slight increase in pixel size arises from the combination of reconstruction scaling and calibration adjustments applied during the processing of projection data.

Table 1
Acquisition parameters for phantom and *in vivo* animal SPECT imaging studies.

Parameters	Phantom and animal imaging
Head Configuration	Dual–Head
Radius of Rotation (mm)	30 – 50
Imaging Mode	Step and shoot
Number of projections	64
Angular Step (Degree)	2.81
Time per View (Sec)	30
Matrix Size	64 x 64
Pixel Size (mm)	1.4 x 1.4

To evaluate the system's quantitative performance, activity concentration measurements were performed in the uniform region and the hot rods of the NEMA image quality phantom. The reconstructed activity concentration, corrected for attenuation, scatter, and resolution recovery, were compared with the known true concentrations to assess quantitative accuracy and recovery performance.

2.10.4. In vivo small-animal studies

To validate the performance and accuracy of the developed quantitative imaging methodology, an *in vivo* animal study was conducted under ethics license no. IR.TUMS.AEC.1403.110 from Tehran University of Medical Sciences. Three healthy male mice were used for this experiment. The animals were anesthetized via subcutaneous injection of a mixture containing 10% Xylazine and 10% Ketamine. Following anesthesia, ^{99m}Tc-DMSA (dimercaptosuccinic acid) and ^{99m}Tc-MAA (Macro Aggregated Albumin) was administered intravenously through the tail vein. Imaging was performed two hours post-injection for renal imaging and 15 min post-injection for MAA lung perfusion imaging using the acquisition parameters outlined in Table 1. To quantify the radiopharmaceutical uptake in the related tissues, the mice were euthanized by administering an overdose of the anaesthetic. The kidneys and lungs were then surgically excised and the activity concentration within the tissue measured using a dose calibrator. Radioactive decay of Tc-99 m was corrected for during the interval between dissection and dose measurement. Finally, the activity concentrations obtained from the dose calibrator was compared with those derived from the reconstructed images to evaluate the accuracy of quantitative imaging.

2.11. Performance evaluation metrics

2.11.1. Full-width at half-maximum (FWHM)

The Full-Width at Half-Maximum (FWHM) represents the spatial spread of a point spread function (PSF) or line spread function (LSF) at half of its maximum intensity. According to SPECT imaging NEMA system performance standards, the FWHM is calculated by first acquiring an image of a point source at a specified distance. The reconstructed image profile, depicting pixel intensity distribution along the image is then plotted. The pixel with maximum intensity and its two adjacent pixels are selected, and a parabolic function was fitted to these three points to determine the profile's peak intensity. Given that the image profile approximates a Gaussian distribution, the points at half-maximum intensity on each side of the peak identified through interpolation. Finally, the average distance between these two points is reported as the FWHM.

2.11.2. Spill-over ratio

The Spill-Over Ratio (SOR) is a key quantitative parameter in SPECT imaging that evaluates both the system's measurement accuracy and the reconstruction algorithm's ability to confine radioactive tracer activity within defined regions without spillover into adjacent areas. Specifically, SOR quantifies the degree of radiotracer leakage from high-activity ("hot") regions into neighboring low-activity ("cold") regions, serving as an important metric for assessing image quantification performance.

For experimental measurements, a NEMA image quality phantom was injected with a standard radiotracer concentration and imaged under standard SPECT acquisition protocols. The obtained projections were reconstructed using the system's standard iterative algorithm. Cold

rod regions within the hot background were then selected as regions of interest to establish high activity-contrast interfaces. Circular ROIs were precisely drawn on both hot background and cold rod regions in multiple transverse slices. The SOR is then calculated as:

$$Spill - OverRatio = \frac{Activityinadjacentcoldregion}{Activityinhotregion} \quad (7)$$

2.11.3. Recovery coefficients

The Recovery Coefficient (RC) quantifies the accuracy of SPECT systems in measuring true activity concentrations, accounting for partial volume effects and reconstruction algorithm performance. The RC is defined as:

$$RecoveryCoefficient = \frac{MeasuredActivityConcentration}{TrueActivityConcentration} \quad (8)$$

Experimental measurements were performed using a NEMA image quality phantom with known activity concentrations. The projections were reconstructed using the quantitative algorithms, and ROIs placed on resolution rods (4–17 mm diameter). RC values were calculated to evaluate system performance across different spatial scales.

For SOR and recovery coefficient (RC) calculations, circular ROIs were defined using a custom ROI tool enabling controlled selection of centre, radius, and slice. ROIs were placed on the central transaxial slice at the visually identified peak of each rod. Diameters of 1.5, 2, 3, and 4 pixels (2.1–5.6 mm) were used to approximate the physical rod sizes while accounting for the 1.4 mm pixel size. RC and SOR values were calculated across all transaxial slices containing the respective structures (hot rods and cold regions), and the reported values correspond to the mean across these slices. Identical ROI definitions were applied across all reconstruction and correction schemes to ensure consistency.

3. Results

3.1. Resolution Recovery

3.1.1. Fitting parameters

To quantitatively characterize the collimator-induced spatial blurring, an experimental study was conducted using a linear rod source positioned at five discrete distances from the detector. Point spread function (PSF) measurements acquired at each distance were used to evaluate the progressive degradation of spatial resolution. The FWHM and standard deviation (σ) of the blurring kernel were extracted from the empirical data.

A linear regression model was applied to the measured FWHM values as a function of source-to-collimator distance, justified by the observed monotonic increase in FWHM with distance. The resulting fitted function enables interpolation of FWHM and σ at arbitrary distances within the operational range. Fig. 2 presents the experimental measurements superimposed with the fitted linear model, demonstrating agreement between empirical data and the theoretical trend.

The derived collimator blurring parameters enable the generation of a physically realistic system matrix that explicitly models the distance-dependent spatial resolution effects. This improved system model yields reconstructed images with enhanced resolution fidelity compared to conventional approaches that approximate collimator response.

3.1.2. Phantom studies

The results of resolution recovery are summarized in Fig. 3 and visualized in Fig. 4.

The derived FWHM trendline from recovered resolutions, obtained through function fitting (FWHM = 0.0447d + 1.362), enables extrapolation to estimate the minimum resolution limit at the detector surface (d = 0). Based on this model, the minimum achievable FWHM at the detector face is 1.3 mm which can be defined as optimal resolution achievable using the HiReSPECT II. Although CDR measurements were obtained up to 90 mm, any required extrapolation beyond this range is minimal and consistent with the expected linear resolution degradation behaviour of parallel-hole collimators.

To evaluate positional dependence of system resolution, a 15 mm off-centred rod source was imaged using the acquisition parameters specified in Table 1. While the nominal radius of rotation (ROR) remained fixed at 45 mm, the effective source-to-detector distances became asymmetric (30 mm to one detector, 60 mm to the opposite detector) due to the off-centre placement. Following resolution recovery processing, the measured FWHM values demonstrated the expected intermediate behaviour between the characteristic resolutions at 30 mm (2.8 mm) and 60 mm (4.1 mm). The off-centred source at 45 mm yielded a recovered resolution of 3.3 mm, confirming that the system's spatially variant resolution performance follows the predicted trend.

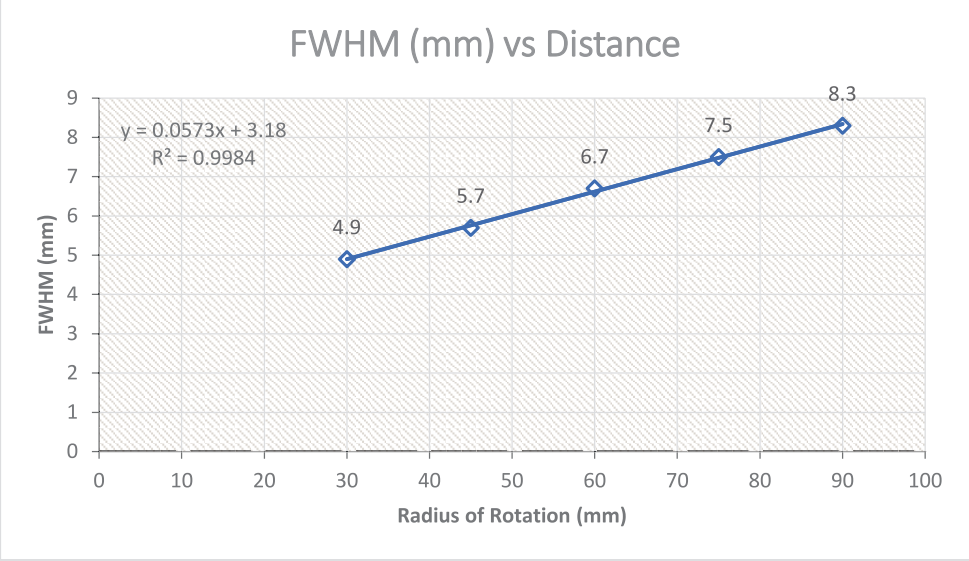

Fig. 2. Empirical characterization of collimator blurring: Measured FWHM (full-width at half-maximum) of the point spread function as a function of source-to-collimator distance (black markers), with linear regression fit (blue line). (For interpretation of the references to colour in this figure legend, the reader is referred to the web version of this article.)

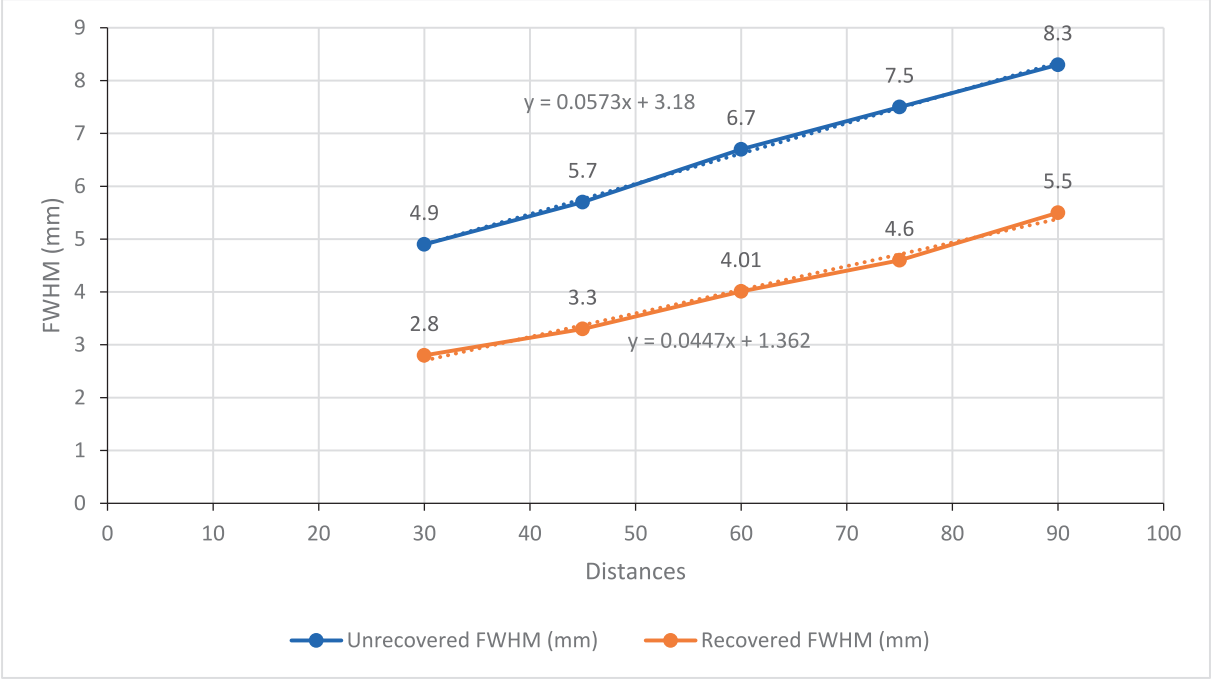

Fig. 3. Comparison of reconstructed spatial resolution (FWHM) with and without CDRF modelling. For each source distance (30, 45, 60, 75, and 90 mm), slices were reconstructed using both a standard system matrix and a CDRF-blurred matrix. The mean FWHM (± standard deviation) across all slices is reported for each reconstruction method, enabling direct evaluation of resolution recovery efficiency.

3.1.3. Attenuation correction

To address photon attenuation effects, Siddon's ray-tracing algorithm was implemented during system matrix generation, modelling attenuation for all projection angles and source-to-detector distances. Reconstructions using the attenuation-corrected system matrix demonstrate improved quantitative accuracy and uniformity, as shown in Fig. 5.

3.1.4. Scatter correction

Scatter correction was implemented using a DEW acquisition protocol. Simultaneous measurements in both the photopeak and scatter energy windows enabled the generation of a scatter projection map, which was then subtracted from the photopeak projection after appropriate weighting. This scatter-corrected projection (Fig. 6, right) demonstrates two key improvements over the uncorrected data: (1) reduced blurring artifacts at phantom boundaries, and (2) enhanced hot-to-cold contrast ratio These corrected projections were subsequently used for image reconstruction.

The proposed framework operates as follows: raw data acquired from the electronic readout board are processed into calibrated projections, followed by scatter correction at the acquisition level and subsequently at reconstruction, resolution recovery and attenuation correction. Fig. 7 demonstrates the performance of this integrated framework using the Animal image quality phantom (resolution section).

3.1.5. Phantom imaging

The calibration factor enables pixel-value-to-activity conversion (KBq/mL) using the known injected activity and phantom volumetry. Quantitative accuracy was assessed in the image quality phantom by comparing image-derived activity ($\sum$[voxel values × CF]) against expected values (concentration × segmented volume) pre- and post-correction. The results presented in Table 2.

3.1.6. Integrated reconstruction framework with data correction

The reconstruction framework must incorporate all three correction steps—resolution recovery (RR), attenuation correction (AC), and scatter correction (SC)—as an integrated process within the reconstruction algorithm rather than as sequential, independent operations. This unified approach ensures optimal image quality by systematically addressing physical degradation factors.

For comprehensive evaluation of quantitative accuracy, both SOR and RC were calculated. These complementary metrics assess different aspects of quantification performance (as detailed in the Methods section). The results are presented in Figs. 8 and 9.

3.1.7. In vivo animal imaging

To enable rigorous quantitative analysis, murine SPECT imaging was performed 2 h after intravenous administration of ^{99m}Tc-DMSA. Immediately after imaging, both kidneys were surgically excised and the absolute radioactivity in each kidney was directly measured using a calibrated dose calibrator (values originally recorded in μCi and converted to Bq for consistency with image-derived units). This ex vivo measurement served as the gold-standard activity concentration for each kidney.

In addition, a separate pulmonary perfusion study was conducted using ^{99m}Tc-MAA in another mice. SPECT acquisition was initiated 15 min after intravenous injection to assess lung uptake under clinically relevant timing conditions.

SPECT-derived activity concentrations were obtained from reconstructed images after (1) application of the calibration factor, (2) adaptive thresholding-based segmentation of renal regions of interest (ROIs), and (3) calculation of activity concentration within the segmented volumes.

Quantitative accuracy was assessed by comparing SPECT-estimated activity concentration against the corresponding *ex vivo* dose-calibrator measurement (gold standard) for each organ separately, using both uncorrected and fully corrected (attenuation-, scatter-, and resolution-recovery-corrected, AC-SC-RR) datasets. The comparison demonstrated substantially improved quantitative accuracy with AC-SC-RR correction. In the right kidney, the absolute percentage error decreased from 17.1% (uncorrected) to 5.8% (fully corrected), representing an 11.3 percentage-point improvement. In the left kidney, the

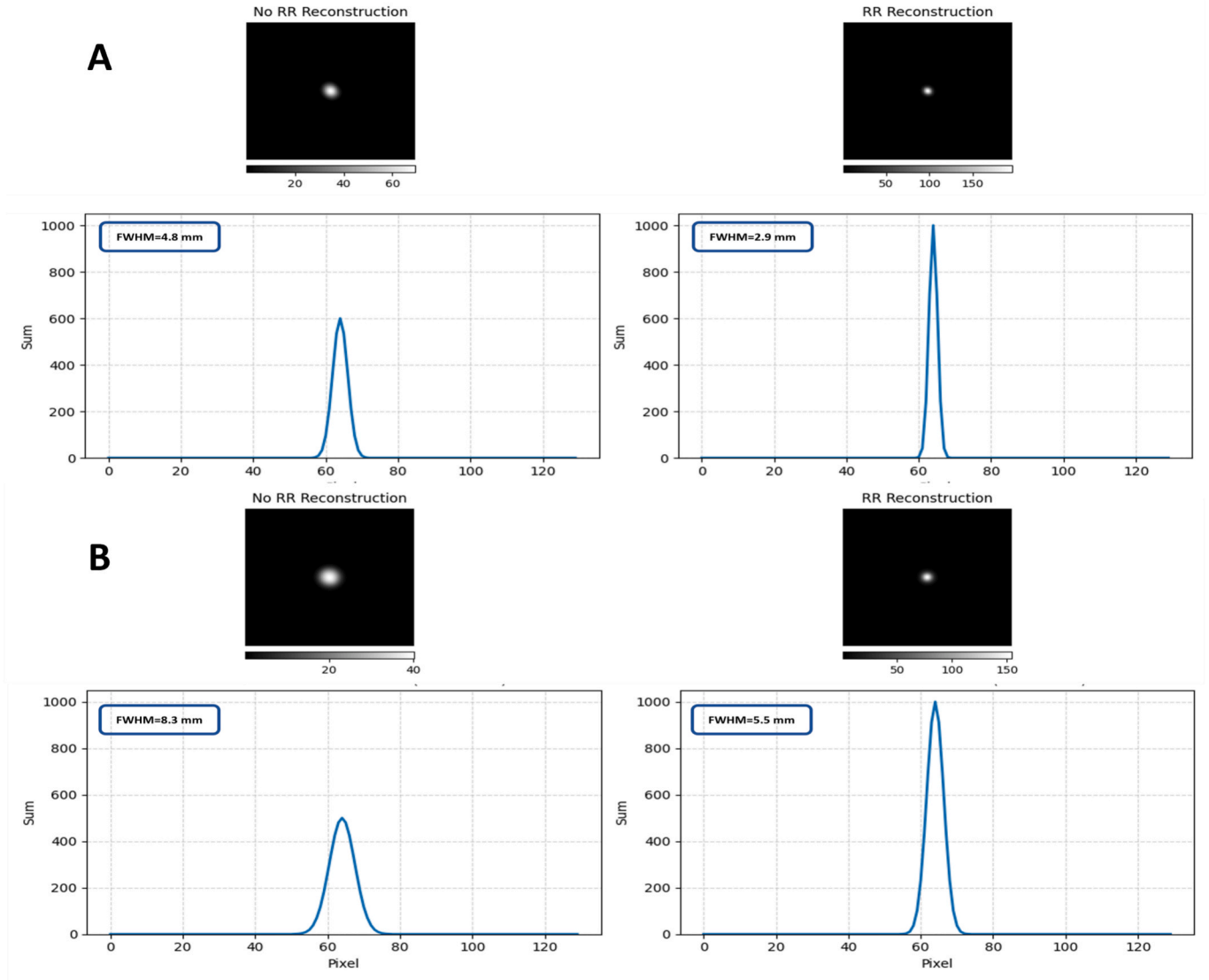

Fig. 4. Comparison of reconstructed rod source images with and without resolution recovery (RR) across 2 distances (A: 30 mm and B: 90 mm). For each distance, the central slice is shown alongside its horizontal line profile, demonstrating the point spread function (PSF) narrowing achieved through RR (CDRF modelling). The line profiles quantitatively illustrate the improvement in spatial resolution (FWHM reduction).

absolute percentage error decreased from 22.6% (uncorrected) to 4.0% (fully corrected), corresponding to an 18.6 percentage-point improvement. Consistent improvements were also observed in the pulmonary perfusion study using ^{99m}Tc-MAA, where the absolute percentage error decreased from 18.1% in the uncorrected images to 4.2% following AC-SC-RR correction. These bilateral results confirm that application of full AC-SC-RR correction markedly enhances the accuracy of renal activity concentration estimates derived from SPECT imaging when validated against direct ex vivo dose-calibrator measurements. A visual comparison of the two reconstruction approaches is presented in Figs. 10 and 11.

4. Discussion

SPECT imaging's quantitative accuracy is fundamentally limited by three physical degradation factors: photon attenuation, Compton scattering, and CDR effects. Our study demonstrated that iterative model-based compensation achieved significant improvements across all domains: (1) CDR modelling in the system matrix reduced the system's FWHM by 33–42% (4.9 mm → 2.8 mm at d = 30 mm), resolving geometric collimator blurring more accurately; (2) dual-energy window scatter correction mitigated false counts (~30% at 140 keV), enhancing lesion edge sharpness, and (3) attenuation compensation eliminated characteristic central cold artifacts, establishing a foundation for absolute quantification. These correlated improvements validate that comprehensive physical modelling is essential for clinical-grade quantitative SPECT.

The demonstrated improvements directly advance quantitative SPECT capabilities in both clinical and preclinical applications. The improved spatial resolution enhanced detection sensitivity for sub-4 mm lesions, overcoming traditional resolution limits imposed by collimator blurring. This enhanced spatial resolution, combined with improved quantitative accuracy (<8% error), enables more reliable uptake measurements for: (1) metabolic bone disease assessment, (2) myocardial perfusion quantification, and (3) precise radionuclide biodistribution studies. Notably, these advancements are particularly valuable for preclinical applications requiring sub-millimeter resolution, such as drug delivery system evaluation and micro-dosimetry calculations in small-animal models.

In comparison with other related studies, Vanhoeve et al. demonstrated that DEW scatter correction combined with μ-map-based attenuation correction significantly improved quantitative accuracy in SPECT imaging. Phantom studies showed a reduction in quantification error

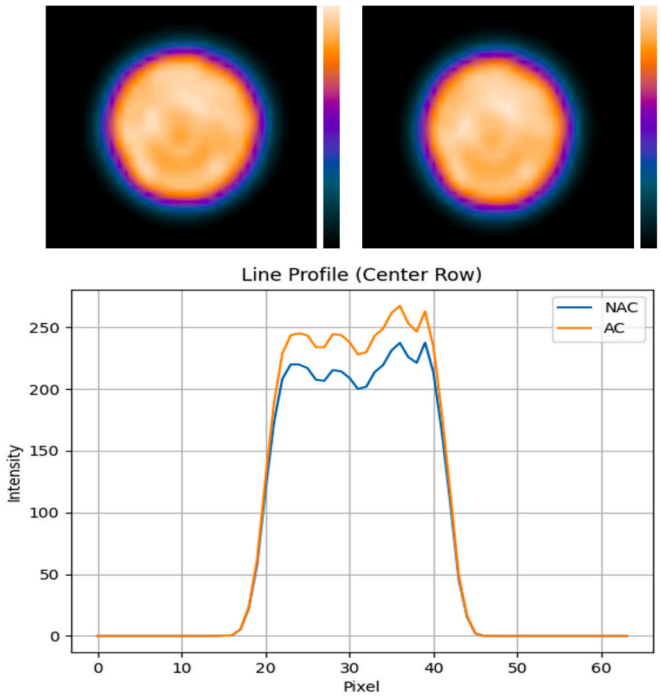

Fig. 5. Attenuation correction effects in a uniform cylindrical phantom. (Top left) Uncorrected reconstruction showing central signal loss due to depth-dependent photon attenuation, quantified in the horizontal line profile (bottom right). (Top right) Attenuation-corrected image demonstrating pathlength-dependent compensation, with the strongest correction observed at central pixels corresponding to maximal source–detector distances.

from − 15.9% to 7.3%, with comparable improvements observed in animal models [38]. Similarly, Khorasani et al. reported that Chang's attenuation correction method enhanced accuracy from − 15.1% to 5.1% in phantoms and from − 22.8% to 3.5% *in vivo* [39]. In human studies, Wu et al. achieved a notable error reduction from −18.7% to −1.7% after applying scatter and attenuation corrections [40]. Our study corroborates these findings, with corrections yielding a mean improvement from − 12.21% to − 1% in phantom evaluations and from − 19.83% to 4.8% in animal studies, underscoring the universal necessity of physical corrections for quantitative SPECT across all scales.

In the present implementation, the collimator-detector response (CDR) was modelled as a distance-dependent 1D radial function embedded within the 2D projection data. This separable approximation captures the dominant radial resolution degradation but does not explicitly model axial resolution loss or inter-slice crosstalk and therefore does not constitute a full 3D system matrix. While a complete 3D model may further improve physical accuracy, radial resolution degradation is the primary spatially varying component in parallel-hole SPECT systems. The adopted 1D distance-dependent formulation therefore represents a practical trade-off between physical completeness and computational feasibility. Similar reduced-dimensional CDR strategies [30] demonstrate near-equivalent quantitative performance compared to higher-dimensional implementations while substantially reducing computational burden.

Attenuation correction in this study was implemented using a uniform water–equivalent coefficient (0.15 cm^{-1}). Although this approach does not explicitly model local high–density structures such as bone, evidence from small–animal SPECT literature indicates that uniform attenuation correction can still provide reliable quantitative accuracy in rodents. For example, Wu *et al.* compared uniform Chang attenuation correction with CT–based non–uniform Chang attenuation in a multi–pinhole small–animal SPECT system and found that the uniform method yielded quantitative results that were highly comparable to non–uniform correction for ^{99m}Tc imaging, with differences generally within a few percent across phantom and animal studies [41]. In addition, Wu *et al.* investigated the effects of inaccuracies in attenuation maps on attenuation–corrected micro–SPECT images and demonstrated that moderate variations in the attenuation map — including coefficient misestimation and small map misalignments — led to relatively small changes in quantitative activity measurements, suggesting that micro–SPECT quantification is robust to such imperfections [42]. Therefore, while CT–based or non–uniform attenuation maps could further refine local quantification, the use of a uniform attenuation coefficient is sufficient to achieve reliable quantitative accuracy in phantom and *in vivo* studies reported here.

This work presents a fully integrated Python-based SPECT reconstruction and quantification platform developed entirely from scratch. The software's modular architecture supports advanced corrections including model-based scatter compensation and attenuation correction, while maintaining compatibility with standardized DICOM data formats. The system's scanner-independent design ensures broad clinical applicability without proprietary constraints. A customizable GUI simplifies complex workflows such as iterative reconstruction tuning and region-of-interest analysis through an intuitive interface. The pure Python implementation guarantees exceptional extensibility for future enhancements, such as AI-based denoising or multi-radionuclide quantification. This combination of technical sophistication and accessibility positions the software as both a powerful research platform for algorithmic developments and a practical clinical solution for quantitative SPECT standardization. Human samples also enabled us to investigate the package scalability and efficient on different data.

The current implementation exhibited several constraints reflecting engineering trade-offs in our initial design. Most notably, the scatter correction module operates at the acquisition level prior to DICOM conversion, requiring proprietary raw data formats from our scanner hardware due to its dependence on specific List-Mode packet architectures. This packet-type sensitivity stems from fundamental requirements in event positioning and energy deposition interpretation that are

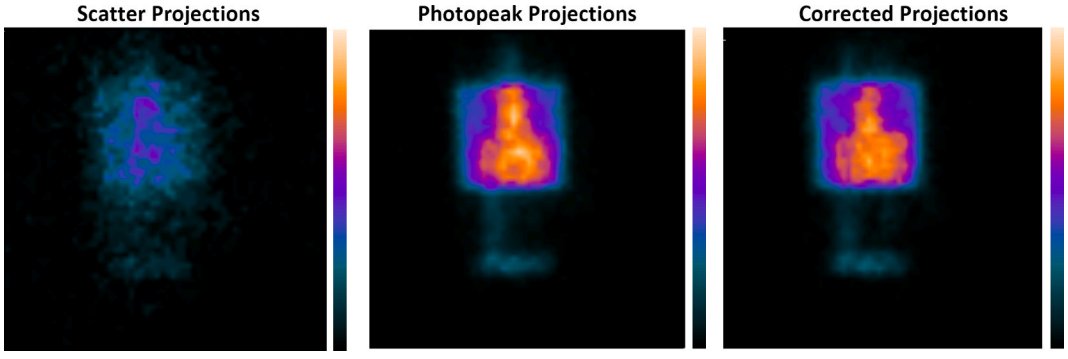

Fig. 6. Scatter window projection (left) – photopeak window projection (middle) – scatter corrected projection (right).

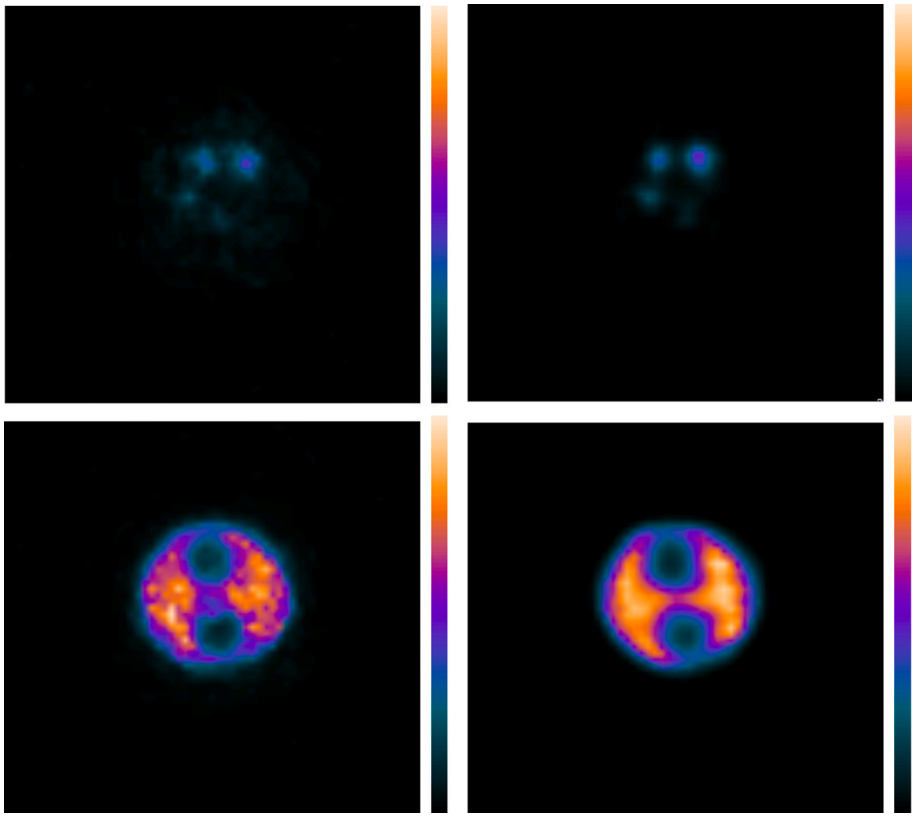

Fig. 7. Animal image quality phantom (Contrast Section (top row) Resolution Section (bottom row)) – The AC-SC-RR reconstructed image (right) demonstrates significant improvements in image quality, including reduced background blurring from scatter correction, enhanced edge definition and fine detail resolution through resolution recovery.

Table 2
Quantitative accuracy assessment of reconstruction methods. Comparison of activity concentration estimates (KBq/cc) and relative errors (%) between: (1) attenuation- and scatter-corrected (AC_SC_RR), (2) uncorrected reconstructions, and (3) gold standard values across phantom regions (uniformity, resolution, and contrast sections).

IQ parts	Gold standard KBq/cc	Uncorrected **Estimated Activity (KBq/cc)**	**Relative Error**	AC_SC_RR **Estimated Activity (KBq/cc)**	Relative Error
Uniformity section	63,717	69,697	9.4%	63,040	−1.0%
Resolution section	5194.3	5747.9	10.7%	5013	−3.5%
Contrast section	29,885	34849.4	16.6%	30653.3	2.6%

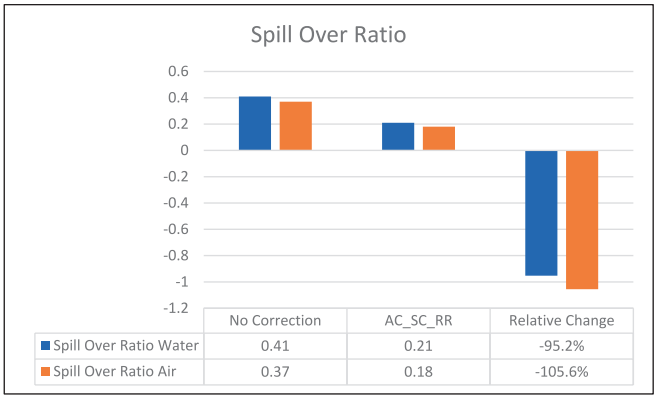

Fig. 8. Evaluation of quantitative accuracy through the Spill Over Ratio factor. After applying corrections, the Spill Over Ratio (SOR) values are observed to decrease. Higher SOR values indicate reduced quantitative accuracy, as they reflect artificial tracer accumulation in areas where no true uptake exists. The reduction in SOR following corrections demonstrates improved quantitative accuracy, as it signifies diminished spurious tracer estimation in inactive regions.

currently hardcoded for our system's data structure. While this optimization ensures maximum performance for our scanners, it temporarily limits the software's compatibility with third-party systems. Additionally, the preprocessing pipeline's position upstream of DICOM standardization introduces workflow constraints for sites using mixed vendor environments. These architectural decisions were necessary to achieve real-time processing during acquisition but will be addressed in future iterations through: (i) development of a post-acquisition DICOM-compatible scatter correction module, (ii) implementation of an adaptive List-Mode parser supporting multiple vendor formats. The existing codebase has been deliberately structured to accommodate these planned extensions without compromising the current optimized processing pathway.

To further enhance quantitative accuracy and clinical applicability, several key advancements are planned: (1) AI-based attenuation map generation will be implemented to improve attenuation correction, particularly for non-homogeneous tissues (e.g., lung/bone interfaces). (2) Advanced scatter correction techniques, including TEW and CT-free attenuation and Monte-Carlo based scatter correction [43], will be developed alongside a post-processing scatter correction algorithm to minimize noise and improve contrast recovery. (3) A fully 3D system matrix will be incorporated into reconstruction to better model photon transport, enabling more accurate 3D SPECT reconstruction. These improvements aim to optimize quantitative precision while maintaining

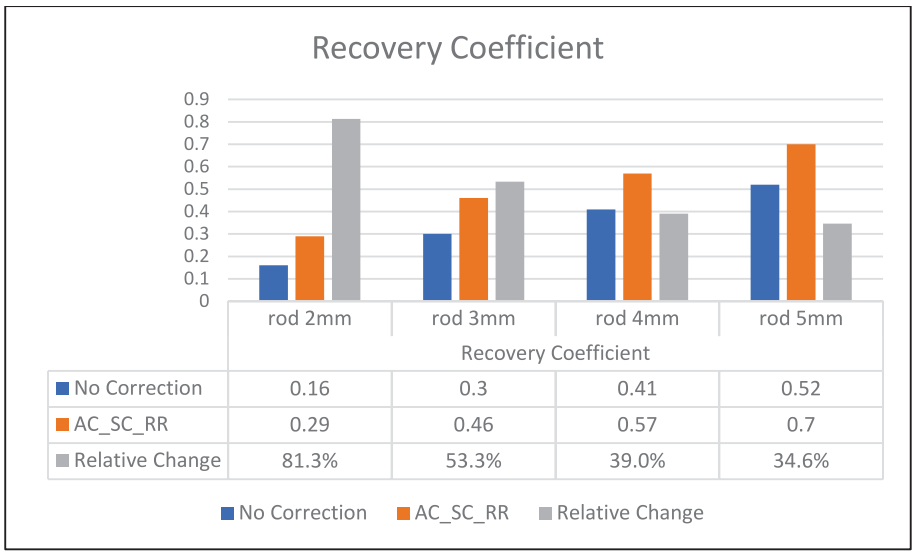

Fig. 9. The recovery coefficient (RC), defined as measured-to-true activity concentration ratio, reflects the accuracy of quantification in small objects. An increase in RC following application of corrections demonstrates reduced partial volume error and improved quantitative accuracy. The relative change in RC for each rod was used to quantify the degree of improvement achieved with the corrections. Although the NEMA phantom includes rod diameters ranging from 1 to 5 mm, the 1 mm rod was not included in the RC analysis. Due to the detector pixel size of 1.4 mm and the intrinsic spatial resolution limitations of the system, the 1 mm rod was below the effective resolution limit and could not be reliably resolved or segmented. Consequently, quantitative RC estimation for this rod was not considered reliable and was therefore excluded from the reported results.

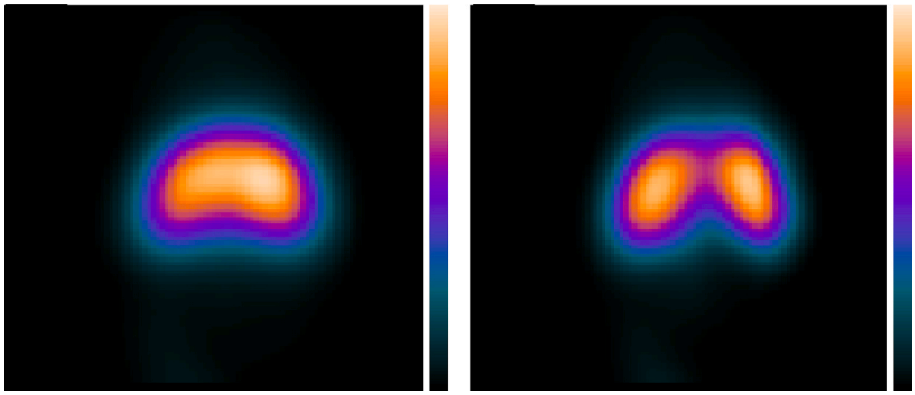

Fig. 10. Comparison of kidney imaging in a mouse model. Coronal views from a DMSA scan demonstrating improved image quality without correction (Left) and with AC-SC-RR reconstruction (Right).

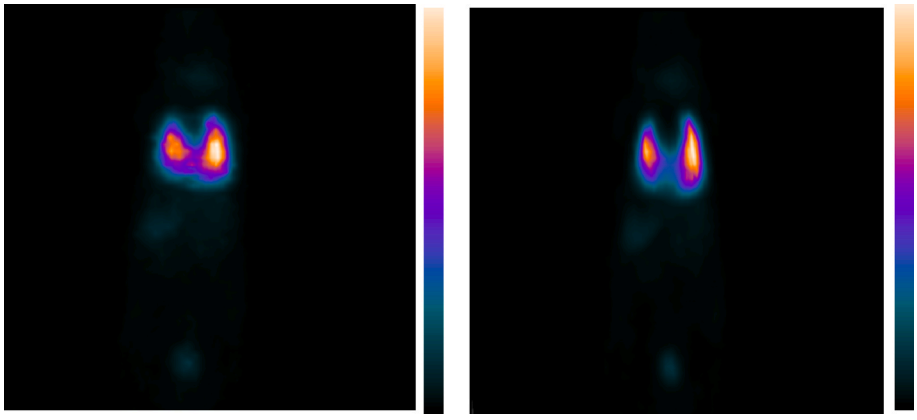

Fig. 11. Comparison of perfusion Lung imaging in a mouse model. 3D modelling of lung scan demonstrating improved image quality without correction (Left) and with AC-SC-RR reconstruction (Right).

computational efficiency for clinical deployment.

5. Conclusion

Preclinical SPECT imaging serves as a vital tool in drug development, radiation dosimetry, and assessing tumor therapeutic response. Accurate quantification of SPECT images is essential in these applications, as precise measurement of radiopharmaceutical uptake directly influences the reliability of experimental outcomes. Achieving such accuracy necessitates corrections for scattering, attenuation, and resolution recovery to ensure that imaging data closely reflects true biological distributions. This study highlights the substantial influence of scattering, attenuation, and collimator effects on SPECT image quality and quantitative accuracy. These factors collectively degrade image quality and introduce errors in quantitative analysis, underscoring the need for systematic corrections. The results demonstrated that iterative reconstruction yielded superior image quality compared to analytical computation, reinforcing its advantage in preclinical SPECT imaging.

In conclusion, this study establishes that accurate quantification in preclinical SPECT imaging requires comprehensive corrections for attenuation, scattering, and collimator effects. Implementing these corrections significantly improved quantitative accuracy, ensuring more reliable and precise outcomes in preclinical research. These findings emphasize the importance of optimized reconstruction techniques to advance the diagnostic and therapeutic applications of SPECT imaging.

Declaration of competing interest

The authors declare that they have no known competing financial interests or personal relationships that could have appeared to influence the work reported in this paper.

Acknowledgements

This work was supported by Tehran University of Medical Sciences under grants no 68594 and 69638 and the Swiss National Science Foundation under grant SNSF 320030_231742.

References

[1] Khalil MM, Tremoleda JL, Bayomy TB, Gsell W. Molecular SPECT Imaging: an Overview. Int J Mol Imaging 2011;2011:796025.
[2] Madsen MT. Recent advances in SPECT imaging. J Nucl Med 2007;48:661–73.
[3] Groch MW, Erwin WD. SPECT in the year 2000: basic principles. J Nucl Med Technol 2000;28:233–44.
[4] Bailey DL, Willowson KP. An evidence-based review of quantitative SPECT imaging and potential clinical applications. J Nucl Med 2013;54:83–9.
[5] Dickson J, Ross J, Voo S. Quantitative SPECT: the time is now. EJNMMI Phys 2019; 6:4.
[6] Bailey DL, Willowson KP. Quantitative SPECT/CT: SPECT joins PET as a quantitative imaging modality. Eur J Nucl Med Mol Imaging 2014;41(Suppl 1): S17–25.
[7] Declercq LD, Vandenberghe R, Van Laere K, Verbruggen A, Bormans G. Drug Development in Alzheimer's Disease: the Contribution of PET and SPECT. Front Pharmacol 2016;7:88.
[8] Son H, Jang K, Lee H, Kim SE, Kang KW, Lee H. Use of Molecular Imaging in Clinical Drug Development: a Systematic Review. Nucl Med Mol Imaging 2019;53: 208–15.
[9] Golestani R, Wu C, Tio RA, Zeebregts CJ, Petrov AD, Beekman FJ, et al. Small-animal SPECT and SPECT/CT: application in cardiovascular research. Eur J Nucl Med Mol Imaging 2010;37:1766–77.
[10] Beller GA, Heede RC. SPECT imaging for detecting coronary artery disease and determining prognosis by noninvasive assessment of myocardial perfusion and myocardial viability. J Cardiovasc Transl Res 2011;4:416–24.
[11] Bernsen MR, Vaissier PE, Van Holen R, Booij J, Beekman FJ, de Jong M. The role of preclinical SPECT in oncological and neurological research in combination with either CT or MRI. Eur J Nucl Med Mol Imaging 2014;41(Suppl 1):S36–49.
[12] Zaidi H, editor. Quantitative analysis in nuclear medicine imaging. New York: Springer; 2006.
[13] Quantitative ZH, Spect,. Recent developments in detector response, attenuation and scatter correction techniques. Phys Med 1996:XII:101–17.
[14] Katsevich A. Theoretically exact filtered Backprojection-Type Inversion Algorithm for Spiral CT. SIAM J Appl Math 2002;62:2012–26.
[15] Shepp LA, Vardi Y. Maximum likelihood reconstruction for emission tomography. IEEE Trans Med Imaging 1982;1:113–22.
[16] Hudson HM, Larkin RS. Accelerated image reconstruction using ordered subsets of projection data. IEEE Trans Med Imaging 1994;13:601–9.
[17] Shaoying L, Farncombe TH. Collimator-detector response compensation in quantitative SPECT reconstruction. IEEE Nuclear Science Symposium Conference Record 2007;2007:3955–60.
[18] Zeraatkar N, Sajedi S, Farahani MH, Arabi H, Sarkar S, Ghafarian P, et al. Resolution-recovery-embedded image reconstruction for a high-resolution animal SPECT system. Phys Med 2014;30:774–81.
[19] Saed M, Mahani H, Sadremomtaz A. Characterization of accurate 3D collimator-detector response function for single- and multi-lofthole collimated SPECT cameras. Jpn J Radiol 2024;42:1330–41.
[20] Sohlberg AO, Kajaste MT. Fast Monte Carlo-simulator with full collimator and detector response modelling for SPECT. Ann Nucl Med 2012;26:92–8.
[21] Ishii K, Hanaoka K, Okada M, Kumano S, Komeya Y, Tsuchiya N, et al. Impact of CT attenuation correction by SPECT/CT in brain perfusion images. Ann Nucl Med 2012;26:241–7.
[22] Patton JA, Turkington TG. SPECT/CT physical principles and attenuation correction. J Nucl Med Technol 2008;36:1–10.
[23] Dietze MMA, Kunnen B, Stella M, de Jong HWAM. Monte Carlo-based scatter correction for the SMARTZOOM collimator. EJNMMI Phys 2020;7:49.
[24] Zhang Y, Chen Y, Zhong A, Jia X, Wu S, Qi H, et al. Scatter correction based on adaptive photon path-based Monte Carlo simulation method in Multi-GPU platform. Comput Methods Programs Biomed 2020;194:105487.
[25] Sakai M, Parajuli RK, Kubota Y, Kubo N, Yamaguchi M, Nagao Y, et al. Crosstalk Reduction using a dual Energy Window Scatter Correction in Compton Imaging. Sensors (Basel) 2020;20.
[26] Michael K, Frangos S, Iakovou I, Lontos A, Demosthenous G, Parpottas Y. The Impact of dual and Triple Energy Window Scatter Correction on I-123 Postsurgical Thyroid SPECT/CT Imaging using a Phantom with Small Sizes of Thyroid Remnants. Life (Basel) 2024;14.
[27] Robinson AP, Tipping J, Cullen DM, Hamilton D. The influence of triple energy window scatter correction on activity quantification for (1 7 7)Lu molecular radiotherapy. Phys Med Biol 2016;61:5107–27.
[28] Mann SD, Tornai MP. Initial evaluation of a modified dual-energy window scatter correction method for CZT-based gamma cameras for breast SPECT. Medical Imaging 2015: image Processing. SPIE 2015:787–96.
[29] Pourmoghaddas A, Vanderwerf K, Ruddy TD, Glenn WR. Scatter correction improves concordance in SPECT MPI with a dedicated cardiac SPECT solid-state camera. J Nucl Cardiol 2015;22:334–43.
[30] Polson LA, Esquinas P, Kurkowska S, Li C, Sheikhzadeh P, Abbassi M, et al. Computationally efficient collimator-detector response compensation in high energy SPECT using 1D convolutions and rotations. Phys Med Biol 2025;70.
[31] Ebrahimifard A, Rajabi H, Geramifar P, Luster M, Yousefi BH, de Nijs R. The impact of the xSPECT reconstruction algorithms on the recovery coefficients value for small tumors: a phantom study with 177Lu. Nuklearmedizin 2025;64:132–40.
[32] Westlund Gotby LEL, Stella M, Van Speybroeck CDE, Lobeek D, van Velden FHP, Stam MK, et al. Towards harmonized holmium-166 SPECT image quality for dosimetry: a multi-center, multi-vendor study. EJNMMI Phys 2025;12:24.
[33] Noori-Asl M, Eghbal M. Comparing the Performance of Scatter Correction Methods in Cardiac SPECT Imaging with Technetium-99m and Thallium-201 Radioisotopes. J Med Phys 2024;49:464–72.
[34] Sajedi S, Zeraatkar N, Moji V, Farahani MH, Sarkar S, Arabi H, et al. Design and development of a high resolution animal SPECT scanner dedicated for rat and mouse imaging. Nucl Instrum Methods Phys Res, Sect A 2014;741:169–76.
[35] Chang LT. A Method for Attenuation Correction in Radionuclide Computed Tomography. IEEE Trans Nucl Sci 1978;25:638–43.
[36] Siddon R. Fast calcuation of the exact radiological path for 3-D CT. Med Phys 1985; 12:252–5.
[37] Jaszczak RJ, Greer KL, Floyd CE, Harris CC, Coleman RE. Improved SPECT quantification using compensation for scattered photons. J Nucl Med 1984;25: 893–900.
[38] Vanhove C, Defrise M, Bossuyt A, Lahoutte T. Improved quantification in single-pinhole and multiple-pinhole SPECT using micro-CT information. Eur J Nucl Med Mol Imaging 2009;36:1049–63.
[39] Gerdekoohi SK, Vosoughi N, Tanha K, Assadi M, Ghafarian P, Rahmim A, et al. Implementation of absolute quantification in small-animal SPECT imaging: Phantom and animal studies. J Appl Clin Med Phys 2017;18:215–23.
[40] Wu C, van der Have F, Vastenhouw B, Dierckx RAJO, Paans AMJ, Beekman FJ. Absolute quantitative total-body small-animal SPECT with focusing pinholes. Eur J Nucl Med Mol Imaging 2010;37:2127–35.
[41] Wu C, de Jong JR, Gratama van Andel HA, van der Have F, Vastenhouw B, Laverman P, et al. Quantitative multi-pinhole small-animal SPECT: uniform versus non-uniform Chang attenuation correction. Phys Med Biol 2011;56:N183–93.
[42] Wu C, Gratama van Andel HA, Laverman P, Boerman OC, Beekman FJ. Effects of attenuation map accuracy on attenuation-corrected micro-SPECT images. EJNMMI Res 2013;3:7.
[43] Mansouri Z, Salimi Y, Wolf NB, Mainta I, Zaidi H. CT-free attenuation and Monte-Carlo based scatter correction-guided quantitative 90Y-SPECT imaging for improved dose calculation using deep learning. Eur J Nucl Med Mol Imaging 2025; 52:3484–99.